

Journal of Biomedical Optics

BiomedicalOptics.SPIEDigitalLibrary.org

Imaging the anterior eye with dynamic-focus swept-source optical coherence tomography

Johnny P. Su
Yan Li
Maolong Tang
Liang Liu
Alex D. Pechauer
David Huang
Gangjun Liu

Imaging the anterior eye with dynamic-focus swept-source optical coherence tomography

Johnny P. Su, Yan Li, Maolong Tang, Liang Liu, Alex D. Pechauer, David Huang, and Gangjun Liu*
Oregon Health and Science University, Casey Eye Institute, 3375 SW Terwilliger Boulevard, Portland, Oregon 97239, United States

Abstract. A custom-built dynamic-focus swept-source optical coherence tomography (SS-OCT) system with a central wavelength of 1310 nm was used to image the anterior eye from the cornea to the lens. An electrically tunable lens was utilized to dynamically control the positions of focusing planes over the imaging range of 10 mm. The B-scan images were acquired consecutively at the same position but with different focus settings. The B-scan images were then registered and averaged after filtering the out-of-focus regions using a Gaussian window. By fusing images obtained at different depth focus locations, high-resolution and high signal-strength images were obtained over the entire imaging depth. *In vivo* imaging of human anterior segment was demonstrated. The performance of the system was compared with two commercial OCT systems. The human eye ciliary body was better visualized with the dynamic-focusing SS-OCT system than using the commercial 840 and 1310 nm OCT systems. The sulcus-to-sulcus distance was measured, and the result agreed with that acquired with ultrasound biomicroscopy. © 2015 Society of Photo-Optical Instrumentation Engineers (SPIE) [DOI: [10.1117/1.JBO.20.12.126002](https://doi.org/10.1117/1.JBO.20.12.126002)]

Keywords: optical coherence tomography; dynamic focus; anterior segment eye imaging.

Paper 150532RR received Aug. 7, 2015; accepted for publication Nov. 2, 2015; published online Dec. 10, 2015.

1 Introduction

Clinically, ultrasound biomicroscopy (UBM) is the standard method for imaging the anterior eye structures behind the sclera, limbus, and iris, which include the ciliary body, crystalline lens, and the lens zonular apparatus. It is utilized for the evaluation of narrow angle, plateau iris, and any lesion in the iris and ciliary body.^{1,2} However, due to the limited axial resolution (about 30 μm for 50 MHz UBM), UBM is unable to reveal the very fine structures and, therefore, cannot provide accurate diagnosis of early-stage tumors.³ UBM is relatively inconvenient due to the need for a coupling gel or liquid to be in contact with eye. A noncontact imaging modality that has deep tissue penetration and high-resolution capability would present a significant improvement.

Optical coherence tomography (OCT) has become a versatile tool for imaging the anterior segment with micrometer resolution in three dimensions.^{3,4} Studies have shown that anterior segment OCT could greatly improve the image resolution compared to UBM.^{1,5} However, OCT has limited penetration due to high signal loss from light scattering in turbid tissue. Another important limitation of anterior segment OCT is the poor depth of focus (DOF) relative to the depth of anterior eye structures—invariably some part of the image is out of focus. For a typical OCT system, the lateral resolution ($\sim\lambda/\text{NA}$) and the DOF ($\sim\lambda/\text{NA}^2$) are correlated, where λ is the imaging wavelength and NA is the numerical aperture of the focusing optics. Increasing the DOF could be realized by trading off the lateral resolution. However, detailed structure provided by higher resolution is always preferred and sometimes essential for early diagnosis of disease.

A few methods have been proposed to increase the DOF for OCT. One method to enhance the imaging depth is the dual beam OCT setup, which has been demonstrated for anterior

eye imaging.^{6,7} The B-frames from dual focal points are combined and processed to improve the imaging resolution across the focal depth. However, this setup requires two interferometers, thus greatly increasing the system cost. Dynamic focus using a liquid lens or deformable mirror, followed by Gabor splicing of image frames, has been demonstrated for optical coherence microscopy (OCM) applications. This technique has shown improved image resolution for the imaging of thick tissues *in vitro* and *in vivo*.^{8–11} Recently, dynamic-focusing OCT imaging has been demonstrated by the use of an acoustic-optical lens and has also improved visualization of the vitreous.^{12,13}

In this study, we will demonstrate a long-range imaging depth (10 mm) of human anterior eye with dynamic-focus swept-source OCT (SS-OCT). Consecutive OCT images at different focal locations achieved by electrically tuning the focal length of a tunable lens can improve imaging penetration depth. Image resolution along the whole imaging range is then enhanced by fusing images obtained at different axial focal planes.

2 Experimental Setup

2.1 Setup of Dynamic-Focus SS-OCT

Figure 1 shows the schematic of the dynamic-focusing SS-OCT system. The swept laser has a central wavelength of 1310 nm, a 100 nm full sweep bandwidth, and a sweeping rate of 50 kHz (Axsun Technologies Inc.). The light from the laser is split by an 80:20 fiber splitter into the reference arm and the sample arm. In the sample arm, the collimated light passes through a telescope formed by an electrical tunable lens (EL-10-30-NIR, Optotune, Dietikon, Switzerland) and a chromatic doublet L2 (focal length 70 mm). After passing through a dual axial galvanometer mirror scanner, the beam diameter was expanded by another telescope

*Address all correspondence to: Gangjun Liu, E-mail: liga@ohsu.edu

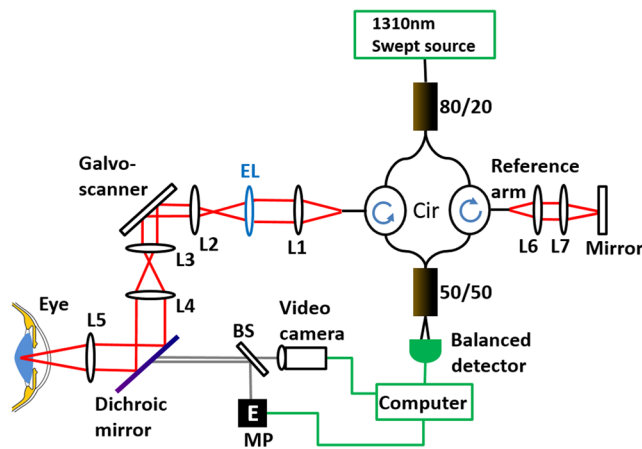


Fig. 1 Schematics of dynamic-focusing swept-source optical coherence tomography (SS-OCT) system. Cir, circulator; MP, miniprojector; EL, electrical lens; and L1–L7 as the lens number from 1 to 7.

(L3 with effective focal length of 30 mm and L4 with effective focal length of 50 mm). After reflecting by a dichroic mirror, the beam is focused by another achromatic double L5 with a focal length of 75 mm onto the sample. The light backscattered from the sample is collected by a circulator and interferes with a reference light reflected from the reference mirror and collected by another circulator. The final interference signal is detected by a balanced photodetector with a bandwidth of 200 MHz (PDB460C, Thorlabs Inc., Newton, New Jersey). The final signal is then digitalized by a high-speed digitizer (ATS9350, Alazar Technologies Inc., Pointe-Claire, QC, Canada). The laser power at the cornea is measured to be 4.59 mW and is within the safety limit set by the American National Standards Institute.¹⁴ The measured system sensitivity is 104 dB around the zero path delay location. The laser provides a clock with a frequency of 91 to 134 MHz. A frequency doubler is used to double the laser clock so that the axial imaging range was extended to around 10 mm in the current setup.¹⁵ The OCT system has a lateral resolution of $\sim 15 \mu\text{m}$ and axial resolution of $8.52 \mu\text{m}$ in tissue. The controlling software can perform automatic focusing, and the operator can switch between dynamic-focusing mode and normal mode. In dynamic-focusing mode, the electrical current applied on the tunable lens was changed automatically for 10 consecutive B-scans, and these 10 consecutive B-scans form a tuning cycle. Within a tuning cycle, the current is tuned from 100 to 390 mA with an increase of 32 mA for each B-scan.

2.2 In Vitro Characterization of Dynamic Focus

In order to test the dynamic-focusing performance of the system, 0.1% intralipid was imaged. The 0.1% intralipid solution was obtained by diluting the 20% stock solution (Sigma-Aldrich) with deionized water. The intralipid solution was held in a cuvette and imaged with the dynamic-focusing mode by the dynamic-focusing SS-OCT system. The results [Figs. 2(a)–2(d)] extracted four B-scan images in a dynamic-focusing tuning cycle, and they show that the system can dynamically change the axial focusing plane. These images show the results when the focal planes are, respectively, at the surface, upper middle, lower middle, and bottom of the sample. Figure 2(f) shows the four normalized A-line profiles extracted from the four representative B-scan images in Figs. 2(a)–2(d). It can be seen that the peak intensity location (which corresponds to the

focal plane location) moves with the changing of electric current to control the lens. The images of the intralipid acquired at different axial focal plane locations are filtered by Gaussian windows to remove the out-of-focus regions part and then averaged to generate a composite image. The final composite image is shown in Fig. 2(e). The axial intensity profile of the composite image is shown in Fig. 2(g), and it can be seen that a strong OCT signal of from 1 to 7 mm is obtained along the axial direction. The composite image in Fig. 2(e) shows the better image quality (higher signal) along the whole image depth.

The sensitivity of the OCT system is proportional to the power returning from the sample. The tissue around the focal plane location will reflect (and scatter) more light due to the high laser power density in the region. So the focal plane region in the OCT image will show better sensitivity. By refocusing the beam into different parts (depths in this setup) of the sample, a higher sensitivity region is tuned accordingly. By combining the high-sensitivity parts of different images acquired from the same sample, a higher sensitivity image is obtained. From Fig. 2(g), it can be found that the composite image combines all the high-sensitivity regions in Figs. 2(a)–2(d) and shows an overall higher signal and better sensitivity. The enhanced sensitivity will allow the OCT system to penetrate deeper. Compared with Fig. 2(a), the composite image in Fig. 2(e) shows increased penetration depth. This increase is a result of using the DOF region in Fig. 2(d). Quantitative analysis shows an increase of more than 20% in penetration depth. This increase is dependent on the focal plane location. The relationship between focal plane depth and the electric current applied to the electrical lens is shown in Fig. 3.

To demonstrate the improvement of lateral resolution along the whole axial imaging range by the dynamic-focusing SS-OCT system, microbeads are imaged. The polymer microbeads (Duke Scientific Corporation, Lot No. 26386) used in this study have a diameter of $9.6 \mu\text{m}$, and they were embedded into 5% (mg/mL) agarose (Sigma-Aldrich, A3893-25G). The sample was held in a cuvette and imaged using the dynamic-focusing mode with the SS-OCT system. Figures 4(a)–4(d) demonstrate the four frames extracted from the images acquired in a focus tuning cycle. The dotted yellow lines in the images indicated the locations of the focusing plane. Due to the limited DOF of the imaging optics, the regions that were out of the DOF in these images were severely blurred, and the microbeads appeared larger or unresolvable in those regions. By filtering of the out-of-DOF regions using Gaussian windows (white curves in the white dashed box overlaid on images) in Figs 4(a)–4(d) and then averaging these filtered images, a composite image as shown in Fig. 4(e) was obtained. A total of nine images were used for averaging to get the composite image in Fig. 4(e), and the white curves overlaid on the image show the nine Gaussian windows that were used to filter the images. Microbeads were clearly resolved along the whole depth range in the composite image. This shows that dynamic-focus OCT can extend the DOF and maintain optimized lateral resolution along the whole imaging depth.

By maintaining the optimum lateral resolution along the whole axial imaging range, the dynamic-focusing SS-OCT improves the lateral resolution for the regions that are out-of-DOF of the focusing optics. The degree of improvement on the lateral resolution for the out-of-DOF region is related to focal plane location and the axial distance of the region to the focal plane. For a Gaussian beam, the beam spot size changes with the propagation of the beam along the beam axis and the beam spot at an axial distance z from the beam focal plane is

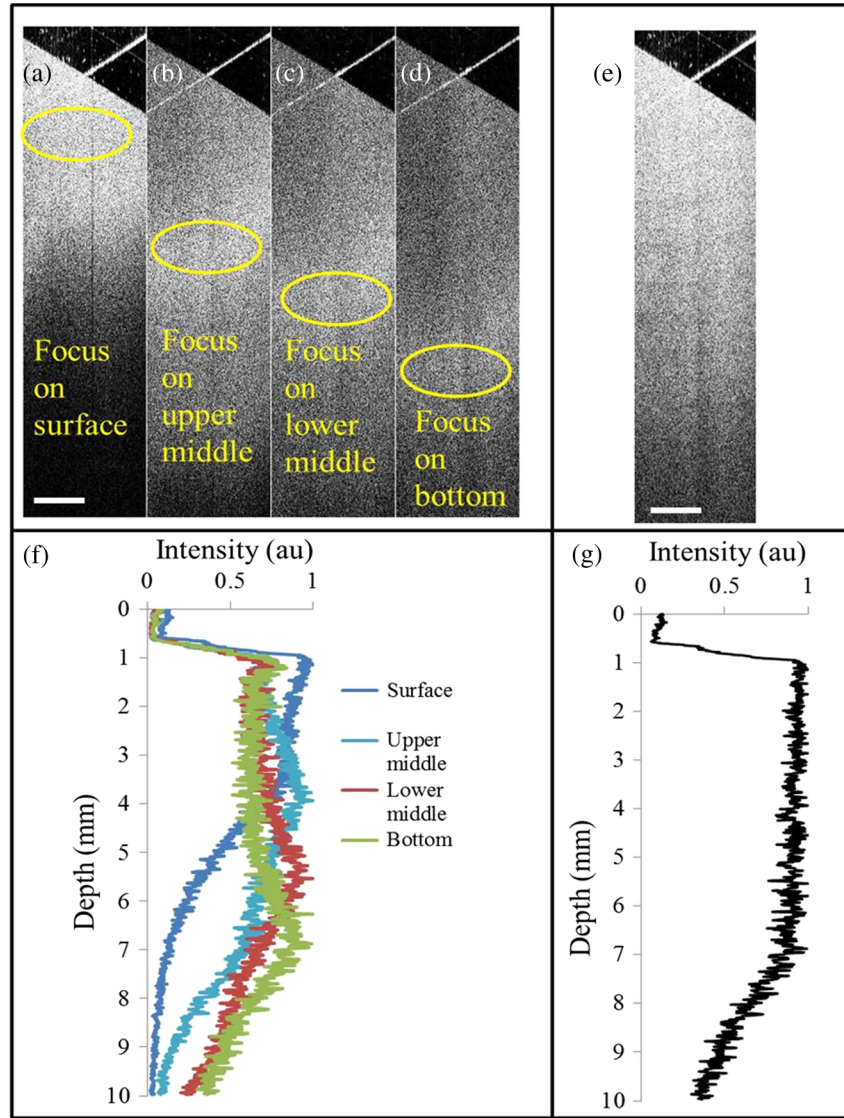


Fig. 2 SS-OCT images of 0.1% intralipid solution obtained at different focal depths. (a)–(d) Images obtained with focal planes at the surface, upper middle, lower middle, and bottom region of intralipid solution. (e) The composite image generated by fusing the Gaussian-weighted window filtering of images (a)–(d). (f) The axial intensity profile for images in (a)–(d). (g) The axial intensity profile for the composite image in (e).

$$w_z = w_0 \sqrt{1 + \left(\frac{z}{z_R}\right)^2}, \quad (1)$$

where w_0 is the beam spot at the focal plane location, w_z is the beam spot at a distance z from the focal plane location, and z_R is the Rayleigh length. So for $z \gg z_R$, the beam spot increases linearly with the distance z . The dynamic-focusing SS-OCT system has a long axial imaging range of 10 mm. For z_R of less than 1 mm in the current setup, the increase of lateral resolution by dynamic focusing can be 5 to 10 times for the out-of-DOF region acquired with the nondynamic-focusing mode.

2.3 In Vivo Imaging and Image Process

This study followed the tenets of the Declaration of Helsinki and was in accord with the Health Insurance Portability and Accountability Act of 1996. The study protocol was approved

by the Institutional Review Board (IRB) of OHSU. The subject in this study was a 25-year-old male with healthy eyes and dark iris pigmentation (brown eyes). Written informed consent was obtained.

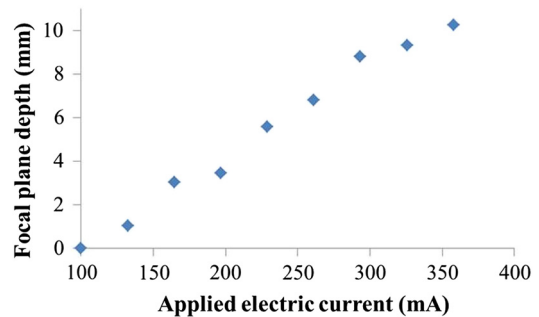


Fig. 3 Relationship between focal plane depth and current applied to the electrical lens.

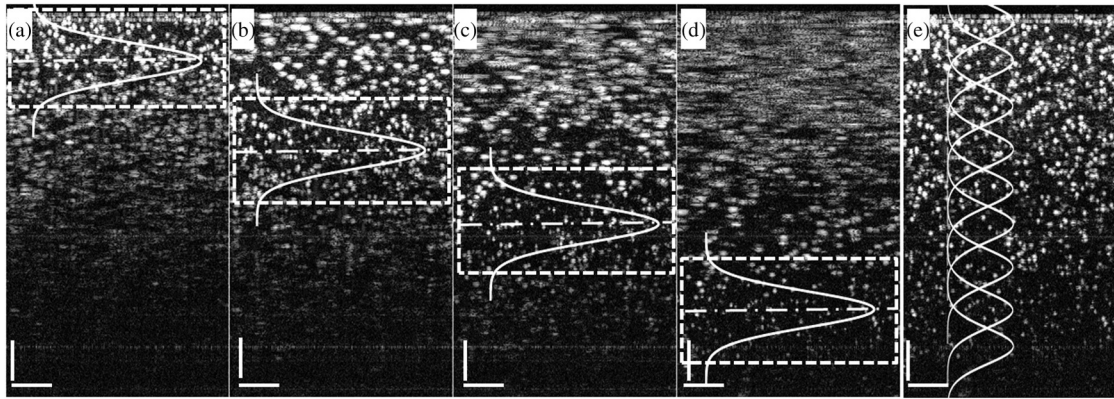


Fig. 4 Imaging microbeads by dynamic-focusing SS-OCT system. (a)–(d) The images of microbeads obtained when the focal planes were set from the surface to the bottom of the cuvette. (e) The composite image by averaging the Gaussian-filtered image frames. Microbeads diameter: $9.6 \mu\text{m}$. The scale bars are 1 mm.

The SS-OCT system was used to image the human anterior chamber *in vivo*. For dynamic-focusing imaging of the sample, 150 repeated B-scan images were obtained in 3 s. Each B-scan frame contained 1024 A-scans and covered a lateral range of about 19 mm. A postprocessing phase stabilization method was used to process the OCT data to eliminate the horizontal line artifacts in the images.¹⁶ The 150 B-scan images were further processed to obtain a high-resolution image. Figure 5 shows the flowchart of the image-processing steps. First, images with large eye motion artifacts were removed from the image set. Then the 10 consecutive frames of one tuning cycle were registered by calculating the cross-correlation between these images [Fig. 5(a)]. The DOF region of each image was selected, and Gaussian window was performed on the region [Fig. 5(a)]. The 10 images were then combined to form a composite, high-resolution image [Fig. 5(a)].^{8,9} The width of the Gaussian

weighting function was 1 mm in our setup. These steps were repeated for different tuning cycles and a few composite images were obtained. A maximum total of 15 composite images could be obtained. Finally, these composite images were registered and averaged to generate a final image [Fig. 5(b)]. A dewarping algorithm was used on the final image to correct the distortion caused by the index transition at the air–tissue interface [Fig. 5(b)].¹⁷

2.4 Compare the Dynamic-Focusing SS-OCT with Time-Domain OCT, Spectral OCT, and UBM

To evaluate the results from our custom-built SS-OCT system, the anterior segment of the normal human subject eye was also imaged using commercially available imaging systems: a TD-OCT system (Visante, Carl Zeiss Meditec Inc., Dublin, California), a spectral OCT system (Avanti, Optovue Inc.,

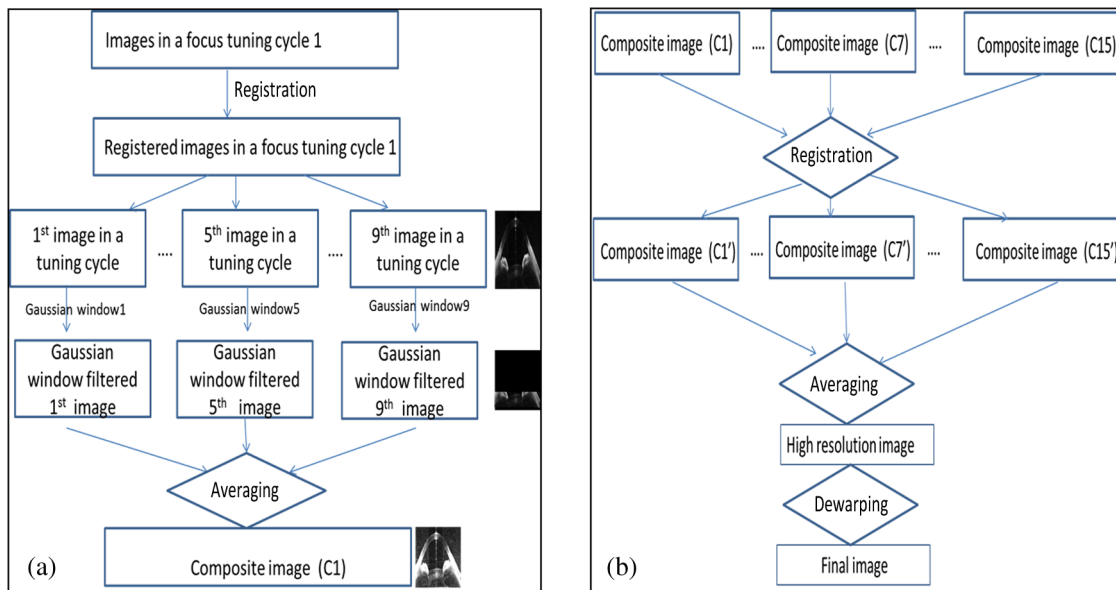


Fig. 5 Flowchart of dynamic-focusing OCT image process. (a) Procedure to get the composite image from the images in a focus tuning cycle. (b) The procedure in (a) is repeated for different tuning cycles to get different composite images. The composite images are further registered and averaged to get a high-resolution image with reduced speckles. The high-resolution image was dewarped to get the final image.

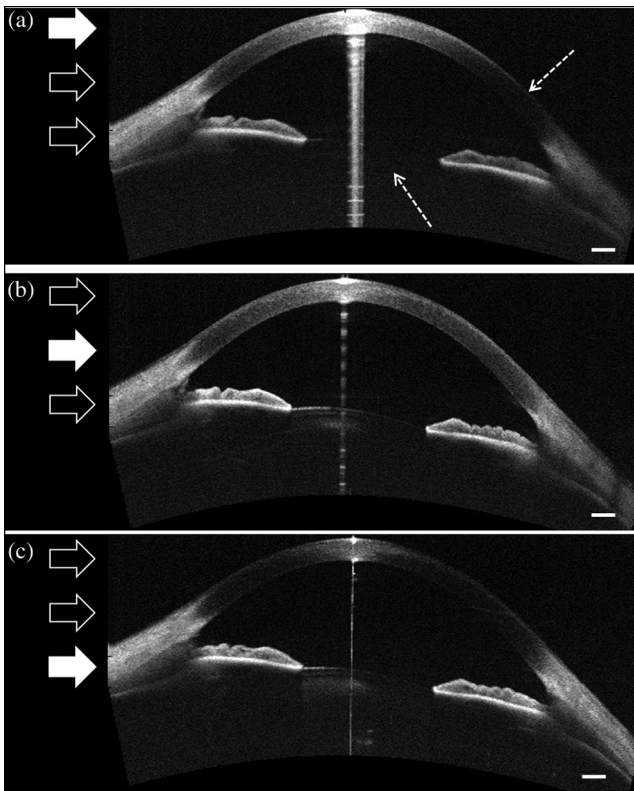


Fig. 6 Imaging of the anterior segment of a normal human subject with manual focus SS-OCT. (a) Focus on anterior surface of the cornea, (b) focus on the middle of anterior chamber, and (c) focus on the anterior surface of crystalline lens. Focal planes are indicated by the solid arrows. The crystalline lens and the periphery part of the cornea (dashed arrows) were not clearly visible when the focusing plane was at the anterior corneal surface (a). These parts were visualized better when the focusing plane moved to the middle of the anterior chamber (b). When the focusing plane was set at the anterior surface of the crystalline lens, the anterior corneal surface signal intensity was low and the crystalline lens signal intensity became higher (c). The scale bar is $500\ \mu\text{m}$ for all images.

Fremont, California), and a UBM (Eyecubed, Ellex Inc., Minneapolis, Minnesota), respectively. The TD-OCT system has a central wavelength of $1310\ \text{nm}$, a speed of $2048\ \text{A-scan/s}$, a lateral resolution of $60\ \mu\text{m}$, and an axial resolution of $18\ \mu\text{m}$. In this study, the anterior segment of the subject was imaged with the built-in scan mode (enhancement anterior segment single scan) in which four B-scan images are registered and averaged. The width of the B-scan was $16\ \text{mm}$, and the axial imaging range in the tissue was $6\ \text{mm}$. The number of A-scans per B-scan for the TD-OCT system was 256. The spectral OCT system used in this study has a central wavelength of $840\ \text{nm}$, a lateral resolution of $22\ \mu\text{m}$, and an axial resolution of $5\ \mu\text{m}$. The width of the B-scan was $8\ \text{mm}$, and the axial imaging range in the tissue was $3\ \text{mm}$. The number of A-scans per B-scan was 1020. A total of 48 B-scan images were registered and averaged. The UBM used in this study has a lateral resolution of $33\ \mu\text{m}$ and an axial resolution of $23\ \mu\text{m}$. The scanning angle was $30\ \text{deg}$ and the axial imaging range in the tissue is $11.9\ \text{mm}$. The acquisition rate was $12.5\ \text{B-scans/s}$. A total of 13 B-scans were used for registration and averaging. The parameters used for different devices in this study are typical clinic setting parameters.

3 Results

3.1 Whole Anterior Chamber Imaging

The anterior chamber of a healthy human subject was first imaged by manually changing the focal plane. The results are shown in Fig. 6. Focal planes were manually tuned from the anterior surface of the cornea to the anterior surface of the crystalline lens as indicated by solid arrows in Figs. 6(a)–6(c). The crystalline lens and the periphery part of the cornea (white dashed arrows) were not clearly visible when the focusing plane was at the anterior corneal surface [Fig. 6(a)]. These parts were better visualized when the focusing plane was at the middle of the anterior chamber [Fig. 6(b)]. When the focusing plane was set at the anterior surface of the crystalline lens, the anterior corneal surface signal intensity was low and

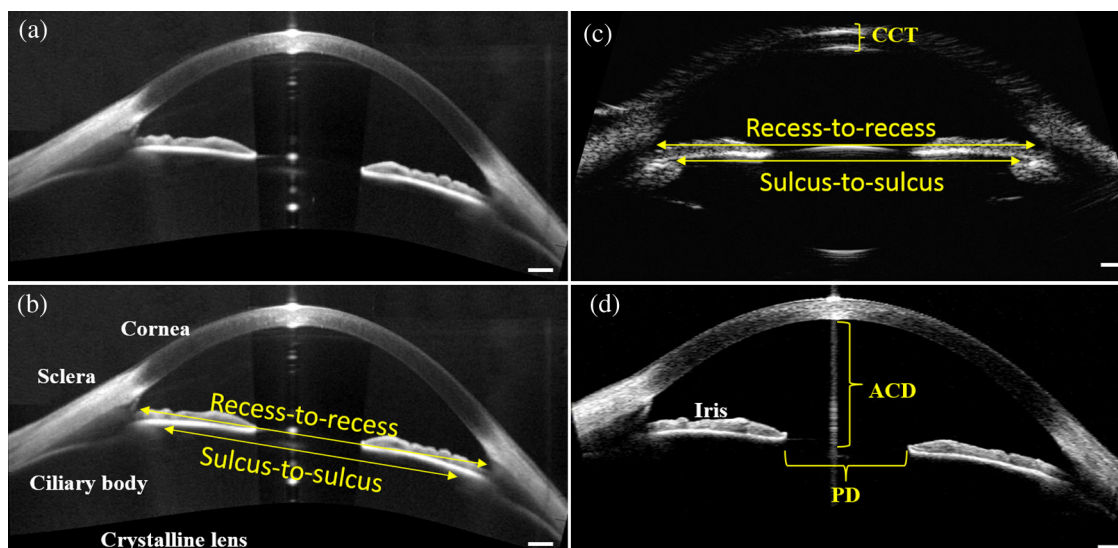


Fig. 7 Imaging of the anterior segment of a normal human subject. (a) and (b) Dynamic-focus SS-OCT images without and with annotation, (c) images obtained with $40\ \text{MHz}$ ultrasound biomicroscopy (UBM), and (d) image obtained with Visante TD-OCT. Both SS-OCT and Visante TD-OCT operate at the 1310-nm wavelength. CCT, central corneal thickness; ACD, anterior chamber depth; and PD, pupil diameter. Scale bars are $500\ \mu\text{m}$ for all images.

the crystalline lens signal intensity became higher [Fig. 6(c)]. It can be seen that the top corneal surface was best visualized in Fig. 6(a). The periphery part of the cornea was best shown in Fig. 6(b). The ciliary body was best demonstrated in Fig. 6(c).

The anterior segment eye of the subject was then imaged using dynamic-focus SS-OCT. The composite image of the anterior segment of a normal human subject was shown in Figs. 7(a) and 7(b). Anterior chamber angle recess, ciliary sulcus, and adjacent structures could be visualized from the image. The sulcus-to-sulcus distance was measured to be 10.93 mm in the 1310 nm SS-OCT image [Fig. 7(b)].

The angle recess and ciliary sulcus were visible on the UBM image [Fig. 7(c)]. The crystalline lens was also visible in the UBM image. The sulcus-to-sulcus distance was measured to be 11.01 mm on the UBM. The angle recess was clear on the TD-OCT, however, the crystalline lens and ciliary sulcus were not visible on the TD-OCT [Fig. 7(d)].

3.2 Transcleral Ciliary Body Imaging

The iris root, trabeculum, ciliary body, ciliary process, and ciliary sulcus could be visualized on the UBM [Fig. 8(a)]. The iris

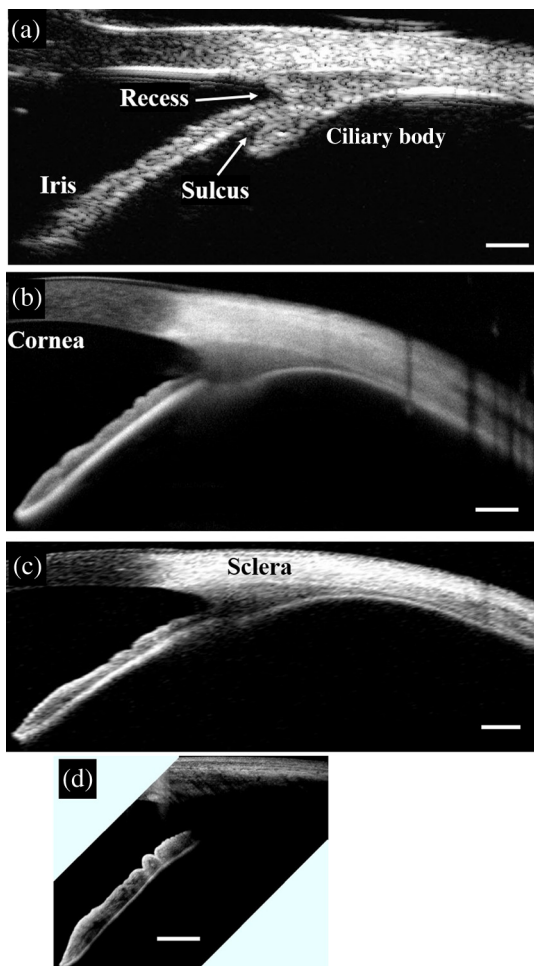


Fig. 8 Imaging of the ciliary body of a normal human subject to UBM and three different OCT systems. (a) Image obtained with 40 MHz UBM, (b) image obtained with dynamic-focus SS-OCT at 1310-nm wavelength, (c) image obtained with Visante TD-OCT at 1310-nm wavelength, and (d) image obtained with spectral OCT at 840-nm wavelength. Scale bars are 500 μm for all images.

root, trabeculum, and most of the ciliary body could be visualized on the 1310 nm dynamic-focus SS-OCT [Fig. 8(b)] and the 1310 nm TD-OCT [Fig. 8(c)], but the ciliary process and sulcus could not be seen. The iris root, trabeculum, and ciliary body cannot be visualized on the 840 nm spectral OCT [Fig. 8(d)]. The contour of the ciliary body epithelium was better defined by the dynamic-focus SS-OCT compared with the UBM.

4 Discussions

Overall, the dynamic-focus SS-OCT system showed better penetration than the 1310 nm TD-OCT and 840 nm spectral domain systems. This is mainly due to the high sensitivity of the Fourier-domain technique used and the reduced scattering loss of the longer 1310-nm wavelength.^{18–20} In addition, the dynamic focus helped to further maintain the lateral resolution along the whole axial imaging range and increase the penetration depth by improving light collection efficiency from selected depths during different phases of focus tuning.¹²

Without dynamic focus, signal level and resolution are poor at the central cornea, midperipheral cornea, or limbus. With dynamic focus, all three regions showed good signal level and resolution. Thus, dynamic focus could be useful in improving the mapping of the entire cornea, at the cost of increased B-scan repetition and imaging time. Since SS-OCT can have very fast scan speeds, this approach for anterior eye OCT will be more attractive as high-speed systems become commercially available.

Despite the limitation of TD-OCT, researchers have used it to measure the horizontal sulcus-to-sulcus distance of an albino patient. In normally pigmented humans, visualization of the ciliary body processes and ciliary sulcus has not been previously demonstrated.²¹ In this study, we demonstrate the imaging of the sulcus-to-sulcus distance for a healthy human participant with brown iris pigment. To the best of our knowledge, this is the first demonstration of using OCT to measure the sulcus-to-sulcus distance for normal eyes. The measurement results agreed well with that obtained by UBM. While our result demonstrated the measurement of sulcus–sulcus distance, the sulcus part of the images is very weak and at the bare limit of visibility. In addition, the dynamic-focus SS-OCT still does not match UBM in terms of image penetration—the ciliary process could be visualized behind the iris, but not behind the sclera. Imaging behind the iris could also be difficult in more darkly pigmented eyes. To further improve the visibility of the sulcus by the dynamic-focusing SS-OCT, the amount of light that is reflected by the sulcus has to be increased and the system sensitivity has to be improved. This could potentially be achieved by increasing the laser power delivered to the cornea (while still maintaining the power within the safety level). Due the sensitivity roll-off of the system, the sulcus demonstrated in this paper was not located at the optimized sensitivity location of the image. If the user prefers to visualize the sulcus better, the sulcus could be placed around the highest sensitivity region of the image (close to the zero path difference location). Another way to improve the sensitivity is to average more images. Of course, this will increase the imaging time.

The current dynamic-focus SS-OCT has several limitations. Although the axial imaging range was 10 mm, the 3 dB sensitivity-roll-off distance was measured to be 5.2 mm. Thus, the signal is reduced for deeper structures. A swept-source laser with a longer coherence length would solve this issue. The electrically tunable lens used in this system is not designed to work

at 1310-nm wavelength. Therefore, the lens coating reduces both signal strength and spectral bandwidth. The axial resolution of the system was decreased by approximately 15% due to limited spectral pass bandwidth of the tunable lens. A spectrometer was used to measure laser source spectrum after the laser passed the tunable lens twice. A 15% reduction of the full-width at half-maximum bandwidth was found for the measured spectrum. A customized lens coating would solve this problem. Overall, improvement in laser coherence length and electrical lens coating could have further improved OCT signal and penetration.

5 Conclusions

A dynamic-focus SS-OCT system with a long axial imaging range has been developed. Enhanced penetration depth and improved lateral resolution along the whole imaging depth have been demonstrated. High-resolution images of the human anterior eye chamber were demonstrated, and the results were compared with several commercially available anterior segment imaging systems. The developed system showed higher penetration depth than the commercial OCT systems used in our study. To the best of our knowledge, we have demonstrated, for the first time, the measurement of sulcus-to-sulcus distance in normal human eyes with OCT.

Acknowledgments

This research was supported by the National Institutes of Health, Bethesda, Maryland (R01EY018184), a start-up fund awarded to Gangjun Liu from Oregon Health and Science Foundation and an unrestricted grant from Research to Prevent Blindness. Dr. David Huang has a significant financial interest in Carl Zeiss Meditec, Inc. (Dublin, California). Oregon Health and Science University (OHSU), Dr. David Huang, Dr. Yan Li, and Dr. Maolong Tang have a significant financial interest in Optovue, Inc. (Fremont, California), a company that may have a commercial interest in the results of this research and technology. These potential conflicts of interest have been reviewed and managed by OHSU.

References

- H. Krema et al., "Spectral-domain optical coherence tomography versus ultrasound biomicroscopy for imaging of nonpigmented iris tumors," *Am. J. Ophthalmol.* **156**(4), 806–812 (2013).
- R. M. Conway et al., "Ultrasound biomicroscopy: role in diagnosis and management in 130 consecutive patients evaluated for anterior segment tumours," *Br. J. Ophthalmol.* **89**(8), 950–955 (2005).
- R. H. Silverman, "High-resolution ultrasound imaging of the eye—a review," *Clin. Exp. Ophthalmol.* **37**(1), 54–67 (2009).
- D. Huang et al., "Optical coherence tomography," *Science* **254**, 1178–1181 (1991).
- S. C. Hau et al., "Evaluation of iris and iridociliary body lesions with anterior segment optical coherence tomography versus ultrasound B-scan," *Br. J. Ophthalmol.* **99**(1), 81–86 (2014).
- Y. Shao et al., "Simultaneous real-time imaging of the ocular anterior segment including the ciliary muscle during accommodation," *Biomed. Opt. Express* **4**, 466–480 (2013).
- C. Zhou, J. Wang, and S. Jiao, "Dual channel dual focus optical coherence tomography for imaging accommodation of the eye," *Opt. Express* **17**, 8947–8955 (2009).
- J. P. Rolland et al., "Gabor-based fusion technique for optical coherence microscopy," *Opt. Express* **18**, 3632–3642 (2010).
- C. Costa et al., "Swept source optical coherence tomography Gabor fusion splicing technique for microscopy of thick samples using a deformable mirror," *J. Biomed. Opt.* **20**(1), 016012 (2015).
- A. S. Lewin et al., "Integrative advances for OCT-guided ophthalmic surgery and intraoperative OCT: microscope integration, surgical instrumentation, and heads-up display surgeon feedback," *PLoS One* **9**(8), e105224 (2014).
- Y. K. Tao, S. K. Srivastava, and J. P. Ehlers, "Microscope-integrated intraoperative OCT with electrically tunable focus and heads-up display for imaging of ophthalmic surgical maneuvers," *Biomed. Opt. Express* **5**(6), 1877 (2014).
- I. Grulkowski, K. Szulzycki, and M. Wojtkowski, "Microscopic OCT imaging with focus extension by ultrahigh-speed acousto-optic tunable lens and stroboscopic illumination," *Opt. Express* **22**(26), 31746–31760 (2014).
- R. Spaide et al., "Improved visualization of the vitreous using swept source optical coherence tomography with dynamic focus sweeping," in *ISIE Imaging Conf.* (2014).
- America, "American National Standard for safe use of lasers," American National Standards Institute, Inc. (2014).
- Z. Wang et al., "Depth-encoded all-fiber swept source polarization sensitive OCT," *Biomed. Opt. Express* **5**(9), 2931–2949 (2014).
- G. Liu et al., "Postprocessing algorithms to minimize fixed-pattern artifact and reduce trigger jitter in swept source optical coherence tomography," *Opt. Express* **23**(8), 9824–9834 (2015).
- D. Huang, Y. Li, and M. Tang, "Interpretation of corneal images," in *Imaging the Eye From Front to Back with RTVue Fourier-Domain Optical Coherence Tomography*, D. Huang, Ed., pp. 39–46, SLACK Incorporated, Thorofare (2010).
- R. Leitgeb et al., "Performance of fourier domain vs. time domain optical coherence tomography," *Opt. Express* **11**, 889–894 (2003).
- J. F. de Boer et al., "Improved signal-to-noise ratio in spectral-domain compared with time-domain optical coherence tomography," *Opt. Lett.* **28**, 2067–2069 (2003).
- M. A. Choma et al., "Sensitivity advantage of swept source and Fourier domain optical coherence tomography," *Opt. Express* **11**, 2183–2189 (2003).
- G. Baikoff et al., "Anterior chamber optical coherence tomography study of human natural accommodation in a 19-year-old albino," *J. Cataract. Refr. Surg.* **30**(3), 696–701 (2004).

Yan Li is an assistant professor of research at the Casey Eye Institute, Oregon Health and Science University. Her research interests include medical image processing, optical coherence tomography (OCT), and OCT angiography for anterior eye.

Maolong Tang is an assistant professor of research at the Casey Eye Institute, Oregon Health and Science University. His research interest includes visual optics, optical coherence tomography, and anterior eye diseases.

David Huang is the Peterson professor of ophthalmology and professor of biomedical engineering at the Oregon Health and Science University (OHSU). He received his MD degree from Harvard and PhD from MIT. He received ophthalmology residency training at the Doheny Eye Institute/University of Southern California and cornea fellowship at Emory University. He is a coinventor of OCT, an imaging technology that has been applied to the measurement of eye structures with unprecedented precision.

Gangjun Liu is an assistant professor at the Casey Eye Institute, Oregon Health and Science University. Before that, he was with BLI, University of California. His research interest is OCT, especially functional optical coherence tomography.

Biographies for the other authors are not available.